Targeted Intraceptor Nanoparticle Therapy Reduces Angiogenesis and Fibrosis in Primate and Murine Macular Degeneration

Ling Luo,[†,‡] Xiaohui Zhang,[†] Yoshio Hirano,[§] Puneet Tyagi,[⊥] Péter Barabás,[†] Hironori Uehara,[†] Tadashi R. Miya,[†] Nirbhai Singh,[†] Bonnie Archer,[†] Yureeda Qazi,[†] Kyle Jackman,[†] Subrata K. Das,[†] Thomas Olsen,[†] Srinivas R. Chennamaneni,[†] Brian C. Stagg,[†] Faisal Ahmed,[†] Lyska Emerson,[∥] Kristen Zygmunt,[#] Ross Whitaker,[#] Christina Mamalis,[†] Wei Huang,[†] Guangping Gao,[▽] Sangly P. Srinivas,[⊗] David Krizaj,[†] Judit Baffi,[§] Jayakrishna Ambati,[§] Uday B. Kompella,[⊥] and Balamurali K. Ambati[†,*]

[†]Moran Eye Center, University of Utah, Salt Lake City, Utah 84132, United States, [‡]Department of Ophthalmology, The 306th Hospital of PLA, Beijing 100101, China, [§]Department of Ophthalmology & Visual Sciences, University of Kentucky, Lexington, Kentucky 40536, United States, [⊥]Skaggs School of Pharmacy, University of Colorado—Denver, Aurora, Colorado 80262, United States, [∥]Department of Pathology, University of Utah, Salt Lake City, Utah 84132, United States, [#]Scientific Computing and Imaging Institute, University of Utah, Salt Lake City, Utah 84132, United States, [▽]Gene Therapy Center, University of Massachusetts, Worcester, Massachusetts 01605, United States, and [⊗]School of Optometry, Indiana University, Bloomington, Indiana 47405, United States

ABSTRACT Monthly intraocular injections are widely used to deliver protein-based drugs that cannot cross the blood-retina barrier for the treatment of leading blinding diseases such as age-related macular degeneration (AMD). This invasive treatment carries significant risks, including bleeding, pain, infection, and retinal detachment. Further, current therapies are associated with a rate of retinal fibrosis and geographic atrophy significantly higher than that which occurs in the described natural history of AMD. A novel therapeutic strategy which improves outcomes in a less invasive manner, reduces risk, and provides long-term inhibition of angiogenesis and fibrosis is a felt medical need. Here we show that a single intravenous injection of targeted, biodegradable nanoparticles delivering a recombinant *Flt23k* intraceptor plasmid homes to neovascular lesions in the retina and regresses CNV in primate and murine AMD models. Moreover, this treatment suppressed subretinal fibrosis, which is currently not addressed by clinical therapies. Murine vision, as tested by OptoMotry, significantly improved with nearly 40% restoration of visual loss induced by CNV. We found no evidence of ocular or systemic toxicity from nanoparticle treatment. These findings offer a nanoparticle-based platform for targeted, vitreous-sparing, extended-release, nonviral gene therapy.

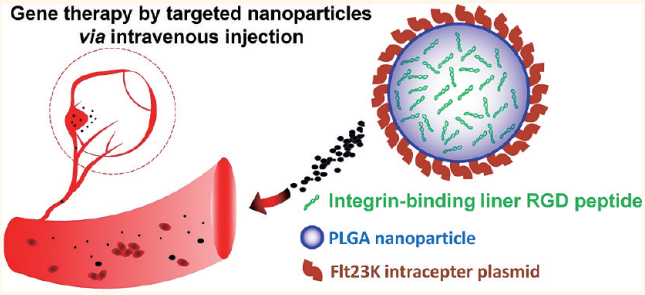

KEYWORDS: nanoparticles · gene delivery · choroidal neovascularization models · anti-VEGF therapy · angiogenesis

Leading retinal causes of blindness (*e.g.*, age-related macular degeneration (AMD),[1−4] angioid streaks, choroidal rupture, and high myopia) share the development of choroidal neovascularization (CNV)—the growth of fibrovascular tissue from the choriocapillaris into the subretinal space—as the underlying etiology of vision loss. Vascular endothelial growth factor (VEGF) plays a central role in CNV development.[5−9] Currently, the primary treatment for CNV consists of monthly injections of antibody-based inhibitors of VEGF into the vitreous.[9−11] Although this therapy improves visual acuity in a substantial proportion of patients, half of the eyes experience ongoing CNV leakage, fibrotic scarring and/or geographic atrophy.[12] Most patients do not experience substantial visual improvement, and a third of treated eyes continue to lose visual acuity and progress to legal blindness.[12] Frequent intravitreal injections represent a significant financial burden and entail risks that include bleeding, infection, traumatic injury, and retinal tear, detachment and degeneration.[9,13] A novel therapeutic strategy which improves outcomes in a less invasive manner, thereby reducing risk, and providing

* Address correspondence to bala.ambati@utah.edu.

Received for review December 23, 2012 and accepted March 6, 2013.

Published online March 06, 2013
10.1021/nn305958y

© 2013 American Chemical Society

TABLE 1. Characterization of RGD.*Flt23k*.NR.NP, *Flt23k*.NR.NP, and Blank.NR.NP[a]

nanoparticle	plasmid loading (% w/w)	particle size (nm ± SD)	polydispersity index (± SD)	zeta potential (mV ± SD)
RGD.*Flt23k*.NR.NP	1.02	572.45 (± 37.43)	0.159 (± 0.027)	−2.11 ± 7.36
Flt23k.NR.NP	1.30	522.91 (± 12.59)	0.111 (± 0.044)	−22.67 ± 7.55
RGD.Blank.NR.NP	NA	163.7 (± 13.3)	0.349 (± 0.08)	− 0.591 ± 0.04
Blank.NR.NP	NA	529.88 (± 29.01)	0.129 (± 0.031)	−27.69 ± 7.10

[a] Data is represented as mean ± SD ($n = 8$).

long-term inhibition of angiogenesis in a lesion-targeted manner is a felt medical need.[14]

Among the potential VEGF inhibitory strategies, anti-VEGF expressing nanoparticles are a promising approcach capable of targeting VEGF intracellularly.[14−17] Advantages of using nanoparticles for gene delivery include sustained delivery, avoidance of viral-induced inflammation, immunogenicity and toxicity, and ease of production.[14,15,17−21] Intracellular VEGF targeting has an advantage in the case of cells responding to their own VEGF secretion in an autocrine fashion, as internal autocrine signaling would not be inhibited by an extracellular VEGF-neutralizing antibody.[22] Autocrine loops have been reported in endothelial cells.[23] The anti-VEGF intraceptor, Flt23K, is a recombinant construct of VEGF binding domain 2 and 3 of VEGFR-1 (vascular endothelial growth factor receptor-1, Flt-1) coupled with the endoplasmic reticulum (ER) retention signal sequence lysine-aspartic acid-glutamic acid-lucine (KDEL).[22,23] KDEL is a peptide retention signal that binds ER retention receptors and prevents secretion of endogenous ER proteins coupled to KDEL. Flt23K intraceptors bind VEGF intracellularly with high affinity and sequester it within the ER, inhibiting VEGF secretion and the VEGF autocrine loop, enhancing the effects of VEGF inhibition.[14,22,23]

CNV also involves subretinal fibrosis, which can adversely affect vision even if angiogenesis resolves. Unfortunately, current treatments for AMD do not address fibrosis. Therefore, combinations of antiangiogenic and antifibrotic factors with long-term effects have been suggested to more effectively improve vision.[24] Integrins are the main mediators of the interaction between fibroblasts and extracellular matrix (ECM) during scar formation. The tripeptide adhesion motif Arg-Gly-Asp (RGD) is contained in the ECM and binds $\alpha v\beta 3$ and $\alpha 5\beta 1$ integrins, which are selectively expressed in areas of neovascularization and scarring.[14,20,25,26] Our previous studies have found that nanoparticles are generally uptaken by cells through phagocytosis and that peptide targeting facilitates uptake by specific cell types.[27,28] Therefore, intravenous delivery of RGD-coated nanoparticles could possibly target anti-VEGF therapy specifically to CNV and reduce fibrosis and angiogenesis while reducing the neural retinal toxicity (*e.g.*, geographic atrophy) associated with intravitreal delivery of extracellular anti-VEGF agents.[12,29]

Laser-induced CNV models are widely used due to their ease of quantification, although laser injury differs from AMD due to the laser's acute injury and retinal burnout with no potential for recovery of visual function. We demonstrated that CNV could be induced by knockdown of sFlt-1 (a soluble isoform of VEGF receptor-1, which acts as a naturally occurring inhibitor of VEGF-A mediated angiogenesis) *via* subretinal injection of adeno-associated viral (AAV) delivery of a short hairpin RNA (shRNA) targeting sFLT-1 (AAV.shRNA.*sFlt-1*).[30] In this study, we further explore whether this model could be used to test visual recovery with inhibition of CNV progression.

We developed an intracellular antiangiogenic therapy relying on a three component system:[14] (1) Plasmids expressing *Flt23k* intraceptors, which consists of the VEGF-binding domains 2−3 of *Flt* (the highest-affinity VEGF receptor); (2) PLGA biodegradable nanoparticles as a delivery system; (3) the tripeptide adhesion motif Arg-Gly-Asp (RGD) to coat nanoparticles and facilitate selective homing to CNV after systemic intravenous injection. We demonstrated that this three component system can inhibit laser-induced CNV in rats.[14] In this study, we further analyzed this targeted nanoparticle system and assessed whether it could regress neovascularization, decrease fibrotic scarring, improve visual acuity, and demonstrate safety profile in two murine CNV models and a primate CNV model.[21]

RESULTS

Nanoparticle Characterization. Characteristics of the nanoparticles are summarized in Table 1 and Figure S1. Plasmid loading in nanoparticles was 1.02 and 1.30% w/w for RGD.*Flt23k*.NR.NP and *Flt23k*.NR.NP, respectively. Mean particle sizes were 572, 523, and 530 nm for the RGD.*Flt23k*.NR.NP, *Flt23k*.NR.NP, and Blank.NR.NP nanoparticles, respectively. Zeta potentials were −22.67 mV, −27.69 mV, and −2.11 mV for *Flt23k*.NR.NP, Blank.NR.NP, and RGD conjugated nanoparticles (RGD.*Flt23k*.NR.NP), respectively. RGD peptide (which contains positively charged amino acids) neutralizes the negatively charged carboxyl groups in the polymer. The size of the RGD.Blank.NR.NP is 163.7 nm (±13.3 nm). Polydispersity is 0.349 (±0.08). The zeta potential is -0.591 mV (±0.04 mV).

We measured the polydispersity index (PDI) of the nanoparticles after preparation and found it to be ~0.100. A low PDI indicates that the particles are of

uniform size, whereas a higher PDI hints at aggregation due to irregular size distribution. Therefore, we speculate that the nanoparticles are not aggregated during preparation and storage. However, the *in vivo* fate of nanoparticles is different. PLGA nanoparticles are rapidly internalized *via* clathrin-mediated endocytosis. Further, modified nanoparticles such as RGD.*Flt23k*.NP can escape early endosomes to reach the cytosol.[27,31] As the PLGA polymer is susceptible to acid hydrolysis, endosomes (having a low pH of 5.0) can deplete the nanoparticles of their surface polyvinyl alcohol (PVA) and cause aggregation. Therefore, *in vivo* conditions can lead to aggregation. The release kinetics result (Figure S2) indicates that the *Flt23k* plasmid is released from RGD.*Flt23k*.NP and *Flt23k*.NP until 42 days and 35 days.

AAV.shRNA.*sFlt-1*-Induced Murine CNV Model. The CNV phenotype induced by subretinal delivery of AAV.shRNA.*sFlt-1* resembles cardinal features of neovascular AMD in humans with regard to its chronicity, progression, and morphology (Figure 1). CNV lesions grew toward the retina, as is observed clinically.[30] Secondary CNV lesions occurred and were separated both in distance and time from primary CNV (Figure 1A). Besides classic CNV, subretinal fluid and intrachoroidal CNV were detected (Figure 1B). These neovascular lesions remained physiologically active even at 6 months postinjection, as indicated by positive isolectin staining (Figure 1C). Therefore, these patterns of CNV progression closely resemble the pathological course of CNV seen clinically in neovascular AMD, and the visual acuity in these eyes could possibly be restored by reversal of architectural changes. However, in laser-induced CNV this restoration is not possible due to partial retina burnout (Figure 1D).

We observed alpha5 integrin expression by immunohistochemical (IHC) staining which demonstrates that alpha5 integrin is expressed strongly in AAV.shRNA.*sFlt-1* induced CNV model, as well as in laser-CNV murine and primate models, suggesting RGD coated nanoparticles could possibly specifically target CNV through the alpha5 integrin recognition sequence RGD (Figure 1E).

RGD-Functionalized Nanoparticles Localize to CNV Lesions. RGD-functionalized PLGA nanoparticles loaded with antiangiogenic plasmid *Flt23k* and conjugated with Nile Red (RGD.*Flt23k*.NR.NP) were detected by the Heidelberg Spectralis imager *in vivo* in CNV eyes and normal eyes (Figure 2A). The nanoparticles were first visualized in retinal blood vessels approximately 30 s following intravenous injection, and thereafter leaked and diffused evenly throughout the retinal vasculature. The higher density of nanoparticles in the fundus was observed for approximately 30 min and then decreased over time and was minimal at 1 h postinjection. More nanoparticles were observed in CNV eyes than in normal eyes (Figure 2A). Upon histological confocal examination of ocular cryosections (Figure 2B) obtained 24 h postintravenous administration of nanoparticles, the nanoparticles were found to be primarily localized to CNV lesions. Nanoparticles were also occasionally observed in normal areas in CNV eyes and normal eyes, primarily in the outer segment layer of the neural retina and retinal pigment epithelium (RPE), with minimal amounts elsewhere in the neural retina. In the murine CNV model, RGD-coated nanoparticles were detected in CNV lesions at 14 days postinjection while in normal eyes nanoparticles were only seen up to 7 days post-treatment (Figure 2B). Consistent with this finding, in monkey CNV models the RGD-conjugated nanoparticles but not unconjugated or blank nanoparticles were detected in CNV lesions at 1 month postinjection (Figure 2C), indicating that RGD modified nanoparticles persisted in CNV lesions for extended periods of time.

RGD Nanoparticles Regress CNV. In the laser-induced CNV monkey model, the average CNV (staining by Perlecan antibodies) volumes were $7.7 \pm 1.0 \times 10^6\ \mu m^3$ ($n = 14$), $13.1 \pm 1.8 \times 10^6\ \mu m^3$ ($n = 16$), $11.4 \pm 0.5 \times 10^6\ \mu m^3$ ($n = 8$) and $20.0 \pm 5.3 \times 10^6\ \mu m^3$ ($n = 19$), in RGD.*Flt23k*.NR.NP, *Flt23k*.NR.NP, Blank.NR.NP, and sham control, respectively. The average fibrosis (staining by Collagen I antibodies) volumes were $0.8 \pm 0.2 \times 10^6$, $1.6 \pm 0.2 \times 10^6$, $1.9 \pm 0.2 \times 10^6$, and $1.9 \pm 0.2 \times 10^6\ \mu m^3$ in RGD.*Flt23k*.NR.NP, *Flt23k*.NR.NP, Blank.NR.NP, and sham control, respectively. This means the CNV volumes at 4 weeks after treatment with RGD.*Flt23k*.NR.NP were less than in controls by 53% ($p = 0.008$), 35% ($p = 0.01$), and 65% ($p = 0.01$), in*Flt23k*.NR.NP, Blank.NR.NP, and sham groups, respectively (Figure 3A). The volumes of fibrosis after RGD.*Flt23k*.NR.NP ($n = 14$) treatment were less than in controls by 53% ($n = 16$, $p = 0.002$), 60% ($n = 8$, $p = 0.005$), and 60% ($n = 19$, $p = 0.0003$) in *Flt23k*.NR.NP, Blank.NR.NP, and sham groups, respectively (Figure 3A).

In addition to suppressing CNV and fibrosis volumes in monkey, RGD.*Flt23k*.NR.NP appeared to substantially reduce the overall volumes of CNV in both the laser-induced and the AAV.shRNA.*sFlt-1* murine models. In mouse laser-induced CNV, the overall volumes of CNV lesions regressed by 24% ($n = 11$, $p < 0.05$) at 2 weeks postintervention in RGD.*Flt23k*.NR.NP, whereas *Flt23k*.NR.NP, RGD.Blank.NR.NP, Blank.NR.NP, and sham controls showed 12%, 8% reduction, 4% increase and 1% reductions in volume, respectively (Figure 3B).There were no statistically significant differences observed among the control groups in both monkey and mouse laser induced CNV models. In the *sFlt-1* knockdown CNV murine model, the overall volumes of the classic CNV lesions at the injection site decreased by 43% ($n = 9$) in RGD.*Flt23k*.NR.NP treated groups. By contrast, CNV lesion volumes increased by 3% ($n = 10$, $p = 0.007$), 33% ($n = 10$, $p = 0.002$), and 54%

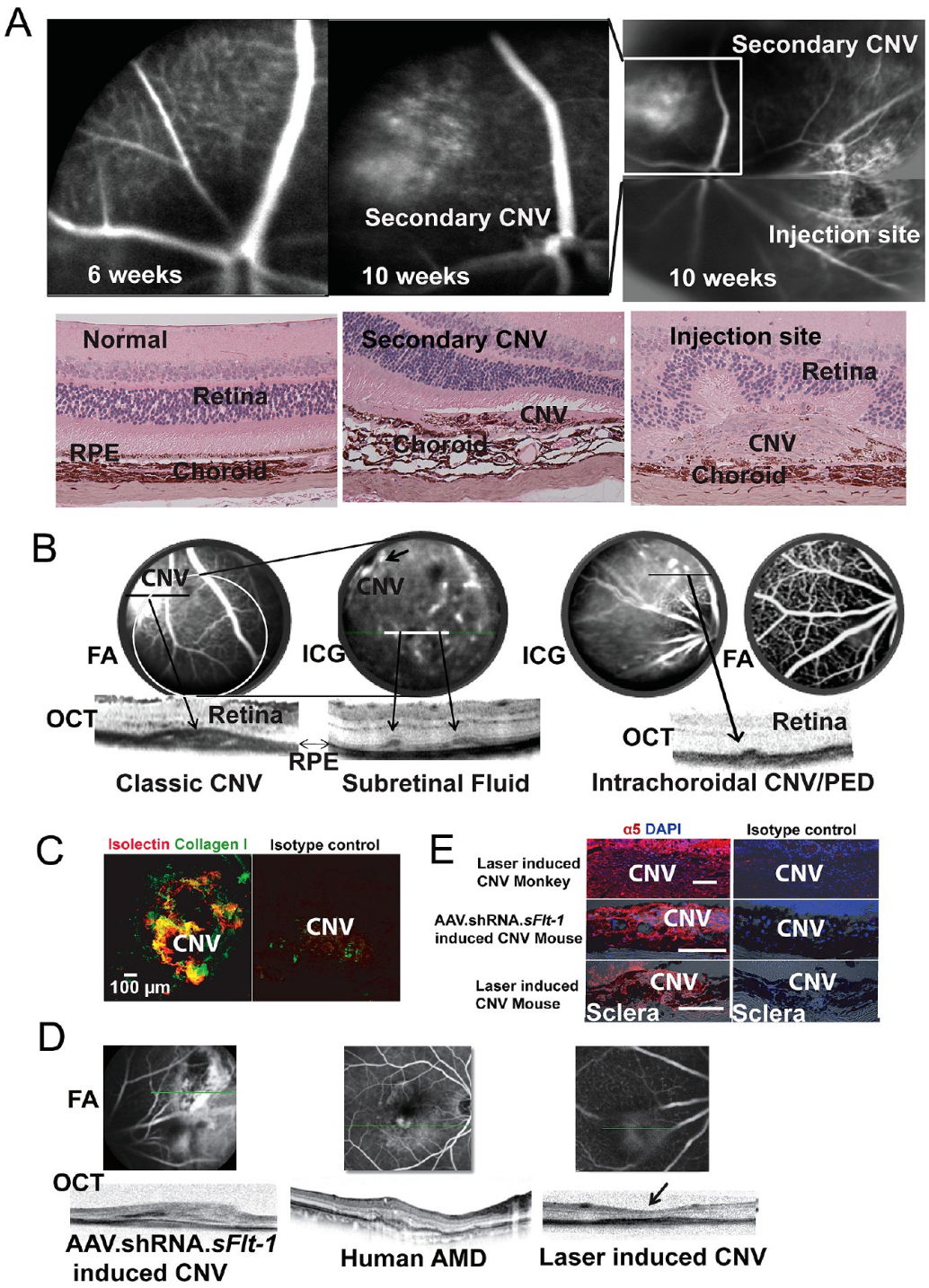

Figure 1. Knockdown (AAV.shRNA.*sFlt-1*) induces murine CNV. (A) Secondary CNV was observed late and distant from injection site on fluorescein angiography (FA, top). Secondary CNV was detected at 10 weeks at a location where CNV was not observed by imaging at 6 weeks after injection and was distant from primary CNV at the injection site. Hematoxylin and eosin (H&E) staining (bottom) shows the histology of normal retina, secondary CNV and classic CNV from the injection site in the *sFlt-1* knockdown mouse (6 months after injection), respectively (40×). (B) Classic CNV, subretinal fluid and intrachoroidal CNV or occult CNV were detected in the same eye (at 6 months). (PED: Pigment epithelial detachment; the top row images are Indocyanine Green (ICG)Angiography images. (C) IHC staining on choroidal flat mounts from *sFlt-1* knockdown eyes (6 months after injection) showed neovessels (isolectin) and fibrosis (collagen I) in CNV site. (D) The morphology of *sFlt-1* knockdown induced CNV closely mimics human CNV (from the database of Heidelberg Spectralis imager), while the retina in laser-induced CNV eyes displays partial burnout (arrow). (E) IHC staining demonstrates that alpha5 integrin was expressed strongly in all three types of CNV models (scale bar: 100 μm).

(n = 10, p = 0.007), respectively, in *Flt23k*.NR.NP, Blank. NR.NP, and sham controls at 4 weeks after treatment (Figure 3C,D). Furthermore, the average fibrosis volume in the RGD.*Flt23k*.NR.NP group (n = 10) was less

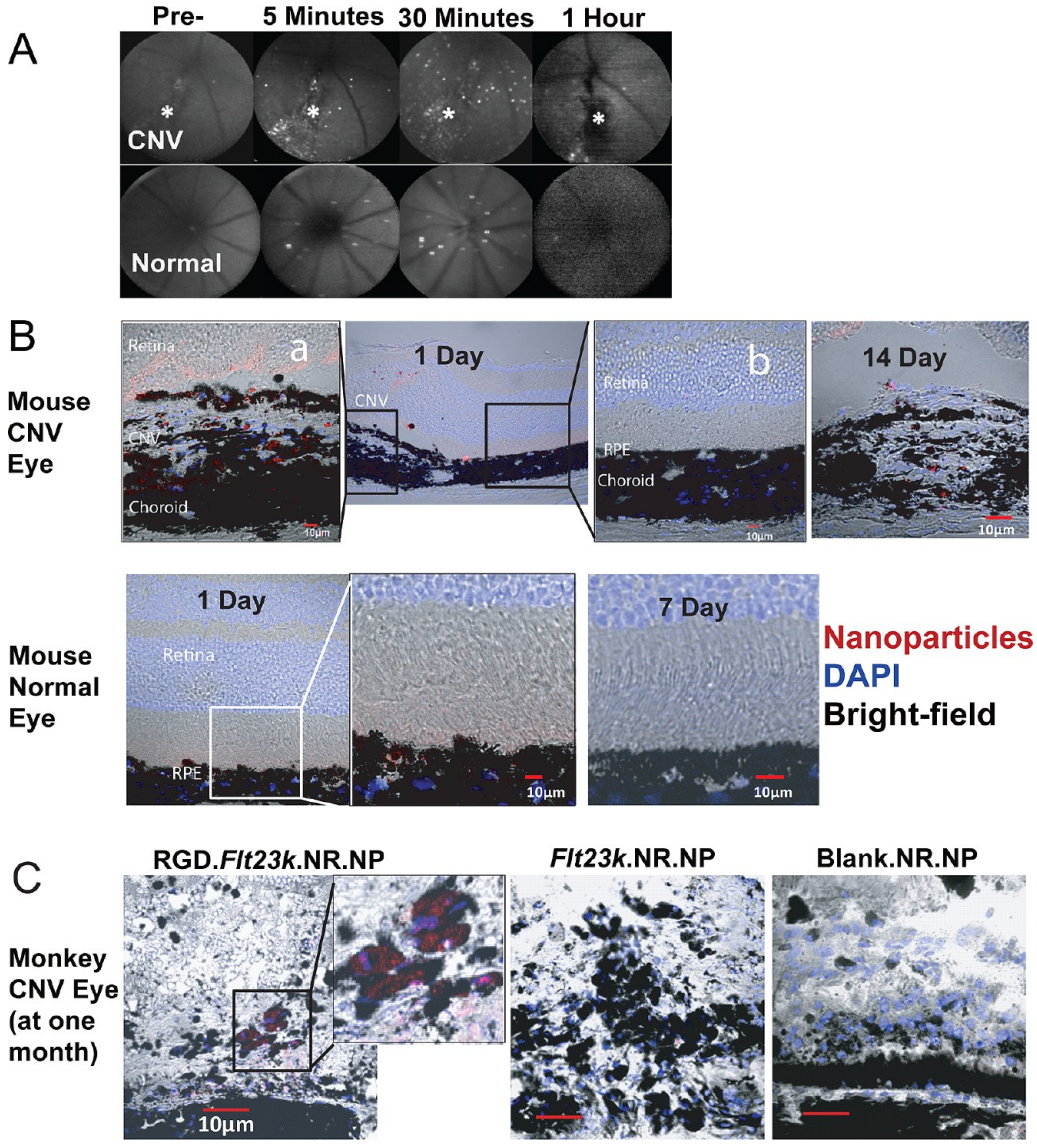

Figure 2. RGD-functionalized nanoparticles localize to CNV lesions. (A) RGD.*Flt23k*.NR.NP was detected by the Spectralis imager *in vivo* in CNV eyes and normal eyes. (B) On histological confocal examination of murine ocular cryosections, more nanoparticles are present in eyes with CNV than in normal eyes. Nanoparticles were concentrated in CNV lesions at 24 h postintravenous injection. RGD-conjugated nanoparticles were detected in CNV lesions 14 days postinjection while only up to 7 days in normal eyes. (a, b) Magnified images from the frames show nanoparticles in CNV site and normal site in the same eye. (C) In laser-induced CNV monkey eyes one month postintervention, some RGD-conjugated nanoparticles could still be detected in CNV lesion. However, unconjugated or blank nanoparticles were not found in CNV lesions.

than that of lesions in the *Flt23k*.NR.NP group by 43.9% ($n = 13$; $p = 0.006$) and by 51.8% *versus* the Blank.NR.NP group ($n = 9$; $p = 0.04$). There was a nonsignificant difference (34.7%) *versus* lesions in the RGD.NR.NP group ($n = 11$; $p = 0.12$) (Figure S3). These results suggest that both angiogenesis and fibrosis are regressed by RGD.*Flt23k*.NR.NP treatment in established CNV, although RGD alone may be effective in ameliorating fibrosis. Furthermore, we observed even more striking results in the AAV.shRNA.*sFlt-1* knockdown CNV murine model. Secondary CNV lesions developed in the controls but not in the mice treated with RGD.*Flt23k*.NR.NP (Figure 3E), indicating RGD.*Flt23k*.NR.NP treatment might inhibit as well as regress CNV. We further compared the efficacy on CNV regression with intravitreal injection of antimouse VEGF antibodies (comparable to clinically used antibody delivery in humans). RGD.*Flt23k*.NR.NP achieved a 24% reduction, which was greater than that achieved with antibody treatment ($n = 10$, 2 weeks, $p < 0.05$, Figure 3F).

Vision Function Is Restored Exclusively after Treatment with RGD.*Flt23k*.NR.NP. As laser-induced CNV models have a limited potential for recovery of visual function due to partial retinal burnout, an AAV.shRNA.*sFlt-1*-induced murine CNV model was used to test visual acuity and the treatments were repeated at 2 weeks post intervention. Whole-head optokinetic tracking (OKT) measurements were performed in a masked manner before

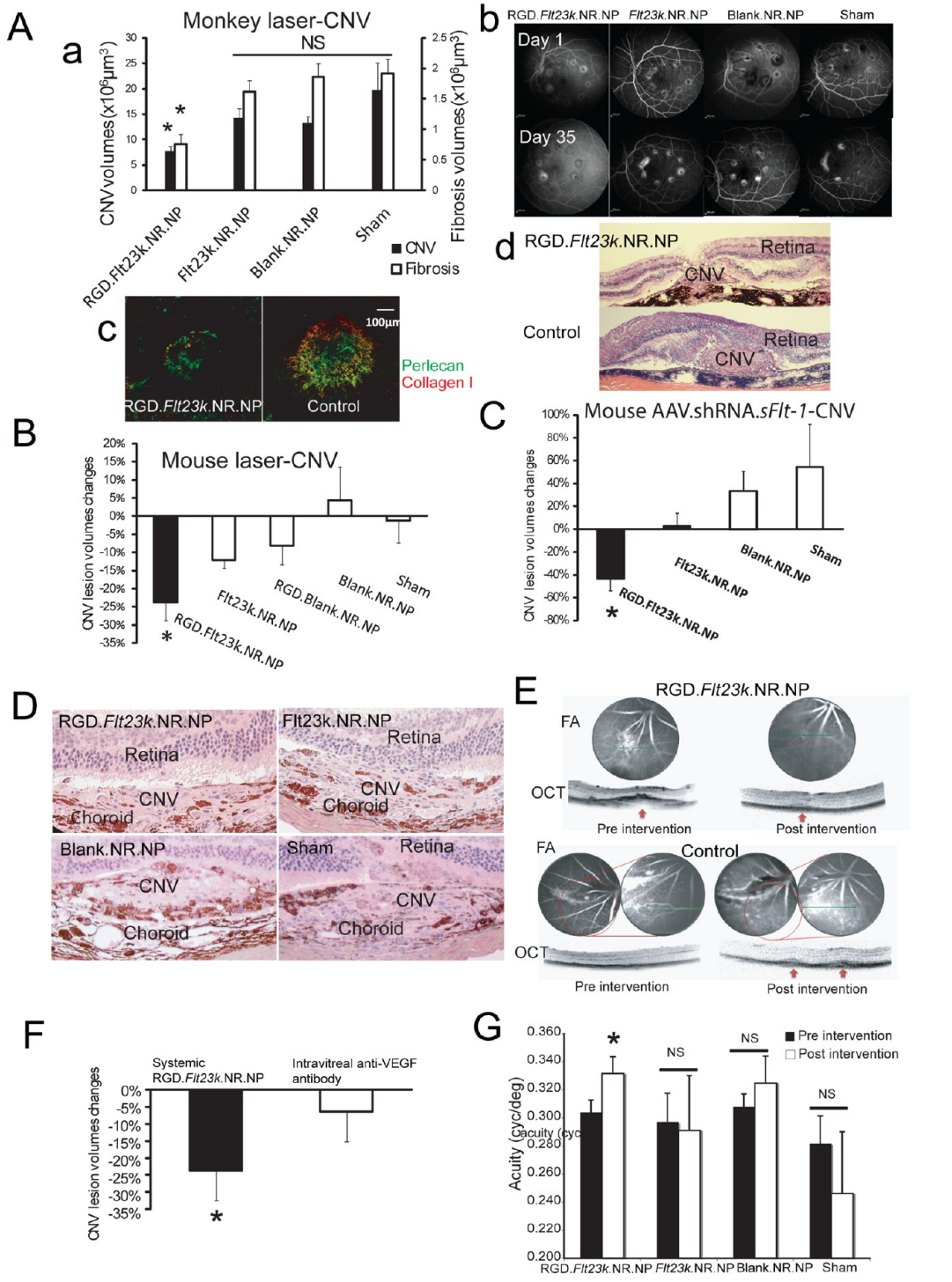

Figure 3. Angiogenesis is inhibited in all CNV models, accompanied by restored vision in CNV eyes induced by *sFlt-1* knockdown. (A) In the laser-induced CNV monkey model, the volumes of CNV lesions, including neovessels (stained by perlecan) and fibrosis (stained by collagen I), significantly decreased 4 weeks after RGD.*Flt23k*.NR.NP treatment (a). Representative images of FA (b), IHC staining(c) and H&E staining (d) show the different size of CNV in each group. (B) In laser-induced CNV mice, CNV lesions were regressed by RGD.*Flt23k*.NR.NP two weeks postintervention. (C) In the *sFlt-1* knockdown induced murine CNV model, the volumes of CNV lesions were significantly decreased by RGD.*Flt23k*.NR.NP at 4 weeks after treatment. (D) Representative FA and OCT images detected the decreased CNV in treated mice from panel C, and detected increased CNV accompanied with secondary CNV occurrence in controls (arrows point to CNV). (E) Representative H&E images of each group in panel C show the different sizes of CNV after intervention. (F) Single systemic administration of RGD.*Flt23k*.NR.NP regressed CNV more than intravitreal anti-VEGF antibody. (G) Optomotor testingvision function was partially restored after 4 weeks treatment with RGD.*Flt23k*.NR.NP but not with the vehicle or sham controls.

treatment and at 2, 4, and 6 weeks post-treatment. All groups of *sFlt-1* knockdown-induced CNV exhibited comparable pretreatment baseline levels of visual acuity (VA) whereas a significant VA increase of 9.4%

was observed following RGD.*Flt23k*.NR.NP treatment (n = 11, p = 0.03, Figure 3G). Gradual yet progressive improvement in behavioral acuity was observed, from ~5% increase at 2 weeks post treatment to ~10% at 4 weeks. At 6 weeks, 85.7% of eyes in the treatment group showed improved VA greater than 10%. In contrast, no significant differences in VA were detected among the *Flt23k*.NR.NP, Blank.NR.NP, and vehicle treated control groups, suggesting that RGD.*Flt23k*. NR.NP nanoparticles effectively restored vision compromised by CNV.

No Ocular or Systemic Toxicity Was Detected. Quantification of Nile Red levels in monkeys' serum (at day 1, 7, 14 and 30 post intravenous administration) indicated its concentrations were below quantification limit (BQL, 0.05 μM,) in all samples at all time points (Figure S4), suggesting that amounts of nanoparticles remaining in the bloodstream 1 day after systemic administration were negligible. Nile Red levels were also assessed from the other collected monkey tissues (kidney, lung, skin, and liver) to estimate the percentage of nanoparticles which remained at day 30 post intervention. In all tissues, the levels of Nile Red were below quantifiable levels, although Nile red could be observed within CNV lesions in the RGD.*Flt23k*.NR.NP group by confocal microscopy (Figure 2C), indicating that NP's were completely eliminated from systemic organs/tissues by 30 days postadministration.

Further, there was no ocular toxicity observed *in vivo* in any of the study animals. Examinations of animal eyes *in vivo* by experienced ophthalmologists using the Heidelberg Spectralis fundus imager revealed no ocular hemorrhage or inflammation, retinal detachment, retinal degeneration or any other abnormalities indicating ocular toxicity. No significant retina morphological abnormalities *via* histological analysis of H&E staining were observed. Further, no retinal apoptosis (assessed by TUNEL staining) was detected in the retina outside the area of CNV lesions in any group at day 30 postinjection (Figure 3 and Figure 4A,B).

A masked experienced pathologist (LLE) performed microscopic examinations of monkey organ tissue sections. The liver, lung, kidney, and skin sections showed no significant histopathological changes at 1 month following intravenous delivery of nanoparticles (Figure 4C). No abnormal health problems or other adverse events were reported in any monkey within 30 days of treatment.

DISCUSSION

In this study, we tested a novel delivery system with nonviral sustained-release gene therapy to treat rodent and primate models of CNV *in vivo*. We demonstrated that RGD targeting significantly enhances nanoparticles localization and concentration in CNV lesions, and that gene delivery of RGD-conjugated nanoparticles delivering plasmids expressing *Flt23k*, but not controls, *via* a single intravenous administration is efficacious in suppressing CNV and fibrosis. Furthermore, in a model of progressive CNV induced by knockdown of endogenous *sFlt-1*, CNV progression was inhibited and vision function was significantly restored after treatment. We observed no systemic or ocular toxicity after nanoparticle administration. Moreover, the data support the conclusion that the *Flt23k* component inhibits neovascularization while the RGD component also suppresses fibrosis, consistent with earlier reports of the activity of this peptide moiety.[26,32,33]

The recombinant gene is driven by a pCMV vector, which is not integrative; we previously confirmed the release of nanoparticles and the expression of Flt23K in the murine cornea by Western blot *in vivo*.[28,34] Nanoparticles expressing the Flt23k recombinant peptide could last for 5−6 weeks after delivery.[28,34] The plasmid works to express Flt23k for 7−10 days in its naked form, and successfully block angiogenesis *in vitro* and *in vivo*.[17,35] In this study, nanoparticles expressing Flt23K after systemic delivery were observed for at least one month in primate eyes with CNV (Figure 2C). However, they are not present in normal eyes or tissues 1 week after delivery (Figure 2B). These characteristics are significant as they have the potential to improve anti-VEGF efficiency, decrease treatment frequency, reduce untargeted tissue and systemic side effects, and improve delivery to target tissues.

These findings bear particular import in light of studies showing that long-term intravitreal nontargeted anti-VEGF suppression is associated with subretinal fibrosis, choriocapillaris abnormalities, and optic nerve or photoreceptor degeneration,[12,36−38] effects which may be mitigated or avoided by our targeted approach and use of RGD. Further, VEGF has been shown to be important for choriocapillaris, cone, and ganglion cell homeostasis; nontargeted VEGF suppression through genetic modification or intravitreal neutralization results in retinal dysfunction, structural damage, and photoreceptor toxicity in a variety of animal models.[39−44] By targeting anti-VEGF therapy to CNV lesions using RGD-conjugated nanoparticles, our strategy would be expected to minimize or avoid these drawbacks. A previous study showed that ranibizumab treatment regressed CNV by approximately about 26% in monkeys,[45] whereas about a 65% regression in monkey CNV lesion volumes was observed in our study. While these studies are not directly comparable, these observations are encouraging, as is our finding that RGD.*Flt23k*.NR.NP achieved significantly more reduction in CNV volume in mice than intravitreal antimouse VEGF antibody injection. Furthermore, as the normal baseline level for C57Bl/6 mice is approximately 0.37 cycles/degree,[46] the 9.4% improvement (from 0.304 ± 0.009 to 0.331 ± 0.012 cycles/degree)

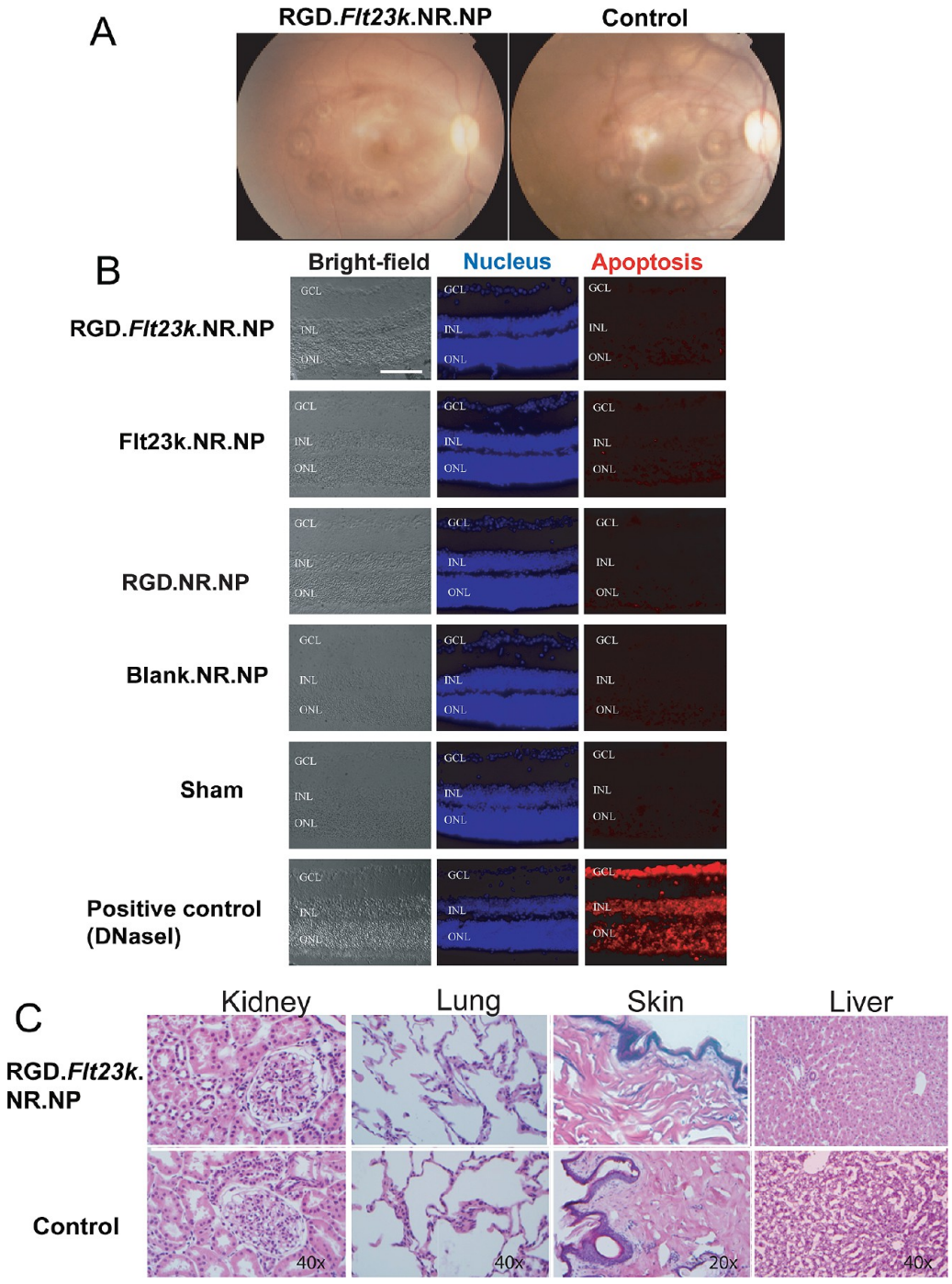

Figure 4. Ocular and systemic toxicity were not detected after RGD.*Flt23k*.NR.NP treatment. (a) Representative monkey ocular fundus images 30 days after intervention showed no significant retinal morphological difference between treatment and control. (B) No apoptosis in the retina outside the CNV lesions was detected at day 30 post intervention by TUNEL staining (scale bar: 100 μm). (C) H&E images showed no significant histopathological changes in the liver, lung, kidney, and skin sections after intravenous delivery of nanoparticles in comparison to untreated, normal organs (30 days).

after targeted RGD.*Flt23k* nanoparticle treatment represents a restoration of approximately 40% of the visual acuity loss due to CNV. Approximately 86% of mice (6 of 7) showed an average improvement of vision by 12.2 $\pm$ 5.2%. In 4 eyes (out of 14) there was an improvement of over 20% and acuity reached 0.371 $\pm$ 0.013 cycles/degree after treatment (baseline acuity in normal mice). This would compare favorably with respect to AMD treatment in humans, where only one-third of patients show overall gain of three lines in visual acuity with intravitreal anti-VEGF injection therapy.[10,12,29]

In this study, we used Flt23k nanoparticles as a stand-alone therapy to determine whether they could take the place of intravitreal anti-VEGF injections, which are used as first-line therapy for choroidal

neovascularization. In earlier work,[47] we have previously used Flt23k nanoparticles in combination with triamcinolone for penetrating keratoplasty (corneal transplant), as triamcinolone is standard of care therapy in corneal transplant, and in that study, we sought to determine whether we could improve transplant success with using our antiangiogenic nanoparticles. We found that the combination of steroids and Flt23k nanoparticles suppressed lymphangiogenesis and hemangiogenesis, synergistically improving transplant survival. Future studies for choroidal neovascularization should explore combination therapies with existing anti-VEGF regimens to see whether the frequency or cumulative dose of intravitreal injections can be reduced.

Although no ocular or systemic toxicity was observed in this study, defects in the eye, kidney, lung, heart, brain, or lungs may be detected after chronic exposure (repeated injections over an extended period of time). Therefore, further studies would be necessary before concluding this delivery system is completely safe.

In conclusion, RGD-targeted nanoparticles delivering *Flt23k* intraceptor plasmids offer a new pathway to ocular drug delivery *via* systemic administration, successfully suppressing neovascularization and fibrosis in models of macular degeneration while avoiding significant drawbacks associated with intraocular injection of anti-VEGF agents.

METHODS

Preparation of Anti-VEGF Intraceptor Plasmid-Loaded PLGA Nanoparticles. PLGA (poly lactide-*co*-glycolide) Resomer 503H (50:50; iv, 0.32−0.44 dL/g; Boehringer Ingelheim Chemicals, Petersburg, VA), Nile Red (Sigma Aldrich, St Louis, MO), and *Flt23k* plasmids were used in the preparation of *Flt23k*.NR nanoparticles. PLGA Resomer 503H (100 mg) was dissolved in 1.75 mL of dichloromethane and Nile Red solution (250 μL of a 1 mg/mL solution in dichloromethane) was added to make up the volume to 2 mL. *Flt23k* plasmid (4 mg) was suspended in TE buffer (500 μL).

The plasmid solution was emulsified with the PLGA solution in dichloromethane containing Nile Red by sonication with a probe sonicator (Misonix Sonicator 3000) at 10 W for 1 min to form the primary emulsion. The primary emulsion was transferred to 10 mL of 2% aqueous polyvinyl alcohol (PVA) solution under sonication at 30 W for 3 min to form the secondary emulsion. The secondary emulsion was kept stirring at room temperature for 4 h. The suspension was further evaporated using a rotovap (Buchi Rotavapor R200; Buchi Analytical, New Castle, DE) for 2 h at 37 °C in a heated water bath (Buchi Heat Bath B490) to remove residual solvent. Following evaporation, nanoparticles were harvested by centrifugation at ∼30 000*g* for 15 min at 4 °C. The supernatant was discarded and the pellet of nanoparticles was redispersed in 25 mL of distilled water. The nanoparticles were recentrifuged at ∼30 000*g* for 15 min at 4 °C. Two such washing steps were performed using distilled water to remove any surface bound PVA and plasmid. The final nanoparticle pellet was redispersed in 10 mL of distilled water and frozen at −80 °C. The frozen dispersion was then subjected to lyophilization (Labconcolyophilizer, Labconco Corporation, Kansas city, MO).

To prepare Nile Red loaded blank particles (Blank.NR.NP), the plasmid was excluded from the procedure described above and TE buffer (without plasmid) was added to form the primary emulsion. Drug content and particle size were characterized for the nanoparticles after lyophilization. Drug content was estimated using UV spectrophotometry, and particle size was measured using Malvern Nanosizer (Malvern Instruments, Ltd., Malvern, U.K.).

To prepare RGD.*Flt23k*.NR nanoparticles, conjugation of the RGD peptide was performed as follows. Plasmid-containing Nile Red-loaded nanoparticles (100 mg, *Flt23k*.NR.NP) were weighed and dispersed in 15 mL of 50 mM MOPS buffer (Sigma Aldrich, St. Louis, MO) by vortexing thoroughly for 15 min. The surface COOH groups were activated by incubation with EDAC (0.01 M, ethyl-3-(3-dimethylaminopropyl) carbodiimide HCl (Sigma Aldrich, St. Louis, MO) at room temperature for 2 h with vortexing. A 10 mM solution of RGD peptide (custom-synthesized by Genscript, Piscataway, NJ) in MOPS buffer (pH 6.5) was added dropwise to activated nanoparticles and vortexed at room temperature for 12 h. Conjugated nanoparticles were separated by centrifugation ∼30 000*g* for 15 min at 4 °C and were lyophilized. The pellet was resuspended in water and lyophilized as described previously.

Nanoparticle Characterization. RGD.*Flt23k*.NR.NP, *Flt23k*.NR.NP, and Blank.NR.NP nanoparticles were characterized for plasmid content, particle size and polydispersity, and zeta potential.

Plasmid content determination: Plasmid loading in RGD.*Flt23k*.NR.NP and *Flt23k*.NR.NP nanoparticles was determined by dissolving 2 mg of the nanoparticles in 1 mL of dichloromethane and extracting the DNA into 1 mL of water. The absorbance of the aqueous layer was measured at 260 nm using a UV spectrometer (Spectramax 250 microplate reader, Molecular Devices LLC, Sunnyvale, CA). Particle size and zeta potential measurement: 1 mg/mL nanoparticle dispersion was prepared in phosphate buffer saline (PBS pH 7.4). This dispersion was subjected to particle size and zeta potential measurement using Malvern Nanosizer (Malvern Instruments Ltd., Malvern, U.K.).

Preparation of Nanoparticles Suspension for Intravenous Delivery. Preparation of nanoparticles suspension for intravenous delivery is described in Supporting Information.

Animals. C57BL/6J mice aged 8−12 weeks purchased from The Jackson Laboratory (The Jackson Laboratory, Bar Harbor, ME) were used for our experiments. Cynomolgus macaque monkeys (3 years of age; male or female, approximately 2.5 kg in weight) were purchased from PreLabs (Oak Park, IL). Experimental groups were age and sex matched. An intravenous catheter was placed in the saphenous vein in the monkeys and routed to a subcutaneous access port for anesthesia and fluorescein administration during the study. The monkeys were fasted overnight prior to treatment and sedated for laser treatment and imaging with ketamine hydrochloride (10−20 mg/kg), atropine sulfate (0.02−0.04 mg/kg), and acepromazine maleate (0.05−0.1 mg/kg) to effect anesthesia. All the mice and monkeys were handled in accordance with the Association for Research in Vision and Ophthalmology (ARVO) Statement for the Use of Animals in Ophthalmic and Vision Research. Experiments were approved by the Institutional Animal Care and Use Committees (IACUCs) of the University of Utah and the University of Kentucky.

***sFlt-1* Knockdown-Induced CNV Models.** *sFlt-1* knockdown-induced CNV models were prepared as described previously.[30] Briefly, small hairpin ribonucleic acid (shRNA) expression cassettes (SECs) were developed by *in vitro* amplification using PCR. SECs are PCR products that consist of promoter and terminator sequences flanking a small hairpin interfering ribonucleic acid (siRNA) template. Multiple target sequences along with different combinations of promoters were screened to find the most effective siRNA capable of gene knockdown *in vitro* and *in vivo*. The best targets for soluble fms-like tyrosine kinase-1 (*sFlt-1*) (AAUGAUUGUACCACACAAAGU) were ligated into the pSEC Neo vector using EcoRI and HindIII (New England Biolabs, Beverly, MA). Plasmids were prepared (Plasmid Mini Prep kit,

Eppendorf, New York City, NY) and sequenced to confirm the in-frame sequence of the inserts. From this plasmid, we developed shRNA.*sFlt-1* and shRNA.Negative cDNA with an H1 promoter. We used pAAV-MCS as a plasmid containing inverted terminal repeat _ENREF_2726, (AAV helper system, Agilent Technologies, Inc., Santa Clara, CA). shRNA.*Flt-1* and sh.Negative cDNA with H1 promoter were inserted to pAAV using PstI site to generate pAAV.shRNA.*sFlt-1* and pAAV.shRNA.Negative. To produce adeno-associated virus (AAV) vector (serotype2), we submitted both plasmids to the Viral Vector Core at the University of Massachusetts.

Mice were placed under general anesthesia with an intraperitoneal injection of tribromoethanol (Avertin) (289 mg/kg). Topical 0.5% proparacaine solution and 1% tropicamide ophthalmic solution were applied to the cornea to achieve topical anesthesia and mydriasis, respectively. Using an Olympus stereomicroscope for magnification, a small incision was made behind the limbus with a 30.5 gauge needle. To deliver AAV.shRNA.*sFlt-1* subretinally, a custom 33-gauge blunt tipped microsyringe (Hamilton Co., Reno, NV) was inserted through the incision and advanced gently across the vitreous behind the lens until it made contact with the neural retina. Gentle pressure was applied to the neural retina puncturing it to enter the subretinal space in the posterior pole. With the needle in position, the AAV vector carrying shRNA.*sFlt-1* was injected into the subretinal space creating a bleb. Dilated fundus examinations during the procedure showed partial retinal detachment seen as a bleb, confirming successful subretinal delivery. The mice were placed on a water circulating heat pad until recovery postprocedure and an antibiotic ointment was applied to the eye.

Laser-Induced CNV Murine and Primate Models. Laser-induced CNV murine and primate models were performed as described in the Supporting Information.

***In Vivo* Monitoring of Nanoparticles and Development of CNV.** *In vivo* imaging of the retinal fundus was performed by Heidelberg Retina Angiography (HRA) and Optical Coherence Tomography (OCT) (Spectralis, Heidelberg Engineering, Vista, CA) using the fluorescein angiograph (FA) and infrared (IR) modes separately. Three-dimensional scanning laser ophthalmoscope (SLO) images of the fundus were obtained using volume scans in the FA mode along with cross-sectional OCT images. SLO images were acquired using the FA mode to visualize the Nile Red loaded nanoparticles after intravenous injection.

Animals were anesthetized and pupils were dilated as described above. Mice were given intraperitoneal injections (0.1 mL) or monkeys were given intravenous injections (0.1 mL/kg) of 10% sodium fluorescein (Akorn, Inc., Lake Forest, IL) to acquire the FA images. Mice were given intraperitoneal injections with 0.2 mL of 8 mg/mL indocyanine green (ICG, Akorn, Inc.) to acquire ICG images. Intravenous administrations of treatment and controls were performed immediately after imaging. Imaging was repeated and recorded by FA+OCT at 2 weeks or 4 weeks after intervention.

Computer-Assisted Quantitative Analysis of OCT Images. Quantification of lesions was performed in a similar approach to previously described techniques for calculating volumes of CNV in humans and retinal blastomas in mouse models.[30,48−50] B-scans were exported from Heidelberg Eye Explorer (HEE), Heidelberg's image analysis software, in .jpeg format and imported as complete stacks into Seg3D software. Seg3D is a segmentation processing and analyzing tool developed by the University of Utah Scientific Computing and Imaging Institute and the NIH/NCRR Center for Integrative Biomedical Computing (Volumetric Image Segmentation and Visualization. Scientific Computing and Imaging Institute, available: http://www.seg3d.org). Boundaries of the CNV lesion and deformations of the RPE were manually outlined using a polyline tool by 2 graders in a masked manner (T.R.M., K.J.). Seg3D masked the region enclosed within the polyline for each consecutive b-scan in pixels squared. An automated feature of Seg3D calculated two-dimensional lesion area, summing the masked b-scans for each stack. Scaling factors obtained from HEE were used to convert pixel^2 to μm^2. After adjusting the corneal curvature to 1.4 mm,[49] the scaling factors for the *x* and *z*-axes were 1.45 $\pm$ 2 and 3.87 μm/pixel, respectively. To calculate lesion volume (μm^3), the spacing between each line scan, the area was multiplied by the distance (52 $\pm$ 2 μm) between scans between scans also provided by HEE software. Finally, estimated volumes were converted to mm^3 and reported.

To quantify the CNV or fibrosis membrane volume using immunostained choroidal flat mounts, horizontal optical sections (3.87 μm/step) were obtained starting from the surface of the RPE-choroid-sclera complex to the deepest focal plane of the choroidal neovascular tuft. Images of each section were stored digitally. CNV or fibrosis was identified by setting a threshold level of fluorescence above which only vessels were captured. The area of CNV or fibrosis-related fluorescence was measured by image analysis software accompanying the microscope. The sum of the entire area of fluorescence in each horizontal section was used as an index of the volume of CNV or fibrosis membrane. Images of each section were stored digitally. The volumes were measured by image analysis software.

Cryosections and Flat Mounts. Cryosections and flat mounts were prepared as described in the Supporting Information.

Immunostaining. To stain CNV or fibrosis, *Griffonia simplicifolia* Alexa Fluor 546 conjugated isolectin (1:200, Life Technologies Corporation, Carlsbad, CA), rat anti-heparan sulfate proteoglycan (Perlecan) monoclonal antibody (1:200, clone A7L6, EMD Millipore Corporation, Billerica, MA), and rabbit polyclonal anti-Collagen I (1:40, Abcam, Inc., Cambridge, MA) were used as primary antibodies. Alexa Fluor488 goat anti-rabbit (1:400, Life Technologies Corporation, Carlsbad, CA) and FITC secondary antibody (1:1000, Anti-Rat IgG-FITC, F6258, Sigma-Aldrich, St. Louis, MO) were used as secondary antibodies. To stain alpha5, rabbit anti-Integrin alpha5 (1:200, EMD Millipore Corporation, Billerica, MA) was used as primary antibody and Alexa Fluor546 goat anti-rabbit (1:200, Life Technologies Corporation, Carlsbad, CA) was used as secondary antibody.

Cryosections were baked at 37 °C for 40 min. Following this, they were washed three times with PBS and then incubated in 10% goat serum (Abcam, Inc., Cambridge, MA) diluted in IHC buffer (1% BSA, 1% FBS, and 0.3% Triton X-100 in PBS [pH 7.4]) for 1 h. They were then incubated with primary antibodies overnight at 4 °C. After primary antibody incubation, slides were washed and incubated in secondary antibodies for 1 h at room temperature (RT). They were then washed 3 times with PBS, after which VECTASHIELD Mounting Medium with DAPI (Vector Laboratories, Inc., Burlingame, CA) was applied and coverslips were placed on the slides. After incubation with secondary antibody in monkey sections, 0.3% Sudan Black (w/v) (Sigma Aldrich, St. Louis, MO) in 70% EtOH (v/v) was applied to slides for 10 min in order to quench the autofluorescence. Slides were then rinsed quickly with PBS 8 times and mounted as above.

To stain murine and monkey flat mount sections, sections were washed twice with PBS for 30 min at 4 °C with shaking. They were then incubated successively in 50%, 75%, and 100% methanol for 30 min each to dehydrate the tissue. This was followed by successive incubation in 100%, 75%, 50%, and 25% methanol at RT for 30 min each to rehydrate the sample. They were then washed 2 times in PBS for 30 min 4 °C, followed by incubation in blocking buffer (1% BSA/0.5% Triton-X/PBS) for 60 min at RT. Primary antibodies were incubated overnight at 4 °C as above. Samples were then washed with 0.1% Triton-X/PBS 3 times for 30 min at 4 °C. As described above, secondary antibodies were then incubated for 2 h at RT, followed by washing with PBS 2 times for 30 min at 4 °C. Sudan Black (0.3%) was then used as above to quench the autofluorescence.

H&E Staining. Samples were sectioned at 1 or 3 μm for H&E staining (described in Supporting Information). All fluorescent sections and H&E stained sections were imaged with an Axiovert 200 microscope (Carl Zeiss Micro Imaging, Inc., Thornwood, NY) equipped with confocal epifluorescence illumination or an Axion Cam MR digital camera (Carl Zeiss Micro Imaging, Inc., Thornwood, NY) and processed using Adobe Photoshop software (Adobe Systems Incorporated, San Jose, CA). Unstained tissue sections were mounted and coverslipped and then directly examined under the above microscopes.

Nile Red Quantification in Serum/Plasma and Organ/Tissues. Nile Red was quantified using dichloromethane (DCM) by liquid−liquid

extraction method as described below. Serum: 0.2 mL of the study sample was transferred to a polypropylene tube and 2.0 mL of DCM was added. All tubes were vortexed for 30 s and centrifuged using Eppendorf centrifuge at 12 000 rpm for 8 min. Organ/tissues: All the collected tissues were weighed and transferred to clean glass tubes; 2.0 mL of DCM was added and homogenized using homogenizer (Polytron 3100D, Kinematica, Inc., Bohemia, NY) at 10 000 rpm for 5 min, to disrupt the tissue and to get a homogeneous suspension. The obtained suspensions were transferred to 2 mL polypropylene tubes after vortexing for 30 s. Tubes were centrifuged at 12 000 rpm for 8 min.

The supernatant was collected from all samples and Nile Red fluorescence was measured by a custom-built fluorometer. The excitation light from a green LED was filtered through 540 + 20 nm interference filter. The emission was collected through a long pass filter at 630 nm and detected by a photomultiplier tube (H5783, Hamamatsu Corp., Bridgewater, NJ). All the study samples were read against a standard calibration curve constructed using known quantities of Nile Red. The curve was linear between 0.05 and 1.0 μM (Figure S4).

Testing Visual Performance. We tested mouse vision using their optomotor reflex, an involuntary head turning in response to the movement of a vertical sinusoidal grating pattern. We used the OptoMotry System (Cerebral Mechanics, Lethbridge, AB, Canada) to display a virtual rotating cylinder of sinusoidal grating created by 4 liquid crystal displays, one on each side of the box. A mouse was placed on a pedestal inside this box with a fixed video camera looking down at it from the top. The video acquisition displayed on the monitor was used to follow and classify mouse movements (tracking *vs* nontracking). Spatial frequency of the stimulus was changed between 0.042 cycles/deg and 0.700 cycles/deg, whereas rotation speed (12 deg/s) and contrast (100%) were kept constant. Spatial frequency of the stimulus was stepped up or down with the staircase method to find the behavioral threshold, corresponding to the visual acuity for the behavior. Tracking was defined as a smooth pursuit movement concordant with the velocity and direction of the stimulus. Trials of each direction and spatial frequency were repeated until the presence or absence of the tracking response could be established unequivocally. Measurements were conducted in masked fashion, *i.e.*, the operator did not know to which experimental group the measured mice belonged.

TUNEL Assay. Enucleated eyes were fixed in 4% PFA/PBS for 2 h at 4 °C, followed by cryoprotection in 15% sucrose/PBS 1 h then changed to 30% sucrose/PBS overnight at 4 °C. Twelve micrometers embedded frozen sections were further processed for TUNEL staining using Click-iT TUNEL Alexa Fluor image assay kit (Cat. No. C10246, Life Technologies, Carlsbad, CA) according to the manufacturer's instructions. A positive control was set up by treatment with DNase I. Retina sections were further counterstained with Hoechst 33342 to identify the retinal cell layers. Inverted fluorescence microscope (Carl Zeiss Micro Imaging, Inc., Thornwood, NY) was used to capture images.

Statistical Analysis. Differences in CNV volumes were compared with the Mann−Whitney U test with Bonferroni correction for multiple comparisons. Two-tailed paired *t* test was used to test optometry in the comparison of before treatment *versus* after treatment data. *P*-values < 0.05 were considered significant. Data are presented as mean ± SEM.

Conflict of Interest: The authors declare the following competing financial interest(s): BA, NS, UK have formal patent applications filed in conjunction with some of the materials described in this paper.

Acknowledgment. We thank Dr. W. Baehr for thoughtful discussions and critical reading of the manuscript. We also thank Dr. R. Marc, J. Ahmed and J. Anderson for technical support. This work was made possible by funding from the National Institutes for Health (NEI 5R01EY017182-04, ER01EY017950-03, P20 RR024215), VAMerit Award. This work is also made in part by EY13870 and The Foundation Fighting Blindness; and software from the NIH/NCRR Center for Integrative Biomedical Computing (2P41 RR0112553-12).

Supporting Information Available: Supplemental methods and supplemental figures (Figures S1−S4). This material is available free of charge *via* the Internet at http://pubs.acs.org.

REFERENCES AND NOTES

1. Ambati, J.; Ambati, B. K.; Yoo, S. H.; Ianchulev, S.; Adamis, A. P. Age-Related Macular Degeneration: Etiology, Pathogenesis, and Therapeutic Strategies. *Surv. Ophthalmol.* **2003**, 257–293.
2. Bunce, C.; Xing, W.; Wormald, R. Causes of Blind and Partial Sight Certifications in England and Wales: April 2007-March 2008. *Eye (London, U.K.)* **2010**, 1692–1699.
3. Jager, R. D.; Mieler, W. F.; Miller, J. W. Age-Related Macular Degeneration. *N. Engl. J. Med.* **2008**, 2606–2617.
4. Pascolini, D.; Mariotti, S. P.; Pokharel, G. P.; Pararajasegaram, R.; Etya'ale, D.; Negrel, A. D.; Resnikoff, S. Global Update of Available Data on Visual Impairment: A Compilation of Population-Based Prevalence Studies. *Ophthalmic. Epidemiol.* **2002**, *2004*, 67–115.
5. Alon, T.; Hemo, I.; Itin, A.; Pe'er, J.; Stone, J.; Keshet, E. Vascular Endothelial Growth Factor Acts as a Survival Factor for Newly Formed Retinal Vessels and Has Implications for Retinopathy of Prematurity. *Nat. Med.* **1995**, 1024–1028.
6. Carmeliet, P.; Jain, R. K. Molecular Mechanisms and Clinical Applications of Angiogenesis. *Nature* **2011**, 298–307.
7. Ferrara, N.; Davis-Smyth, T. The Biology of Vascular Endothelial Growth Factor. *Endocr. Rev.* **1997**, 4–25.
8. Ferrara, N.; Gerber, H. P. The Role of Vascular Endothelial Growth Factor in Angiogenesis. *Acta Haematol.* **2001**, 148–156.
9. Gragoudas, E. S.; Adamis, A. P.; Cunningham, E. T., Jr.; Feinsod, M.; Guyer, D. R. Pegaptanib for Neovascular Age-Related Macular Degeneration. *N. Engl. J. Med.* **2004**, 2805–2816.
10. Brown, D. M.; Kaiser, P. K.; Michels, M.; Soubrane, G.; Heier, J. S.; Kim, R. Y.; Sy, J. P.; Schneider, S. Ranibizumab Versus Verteporfin for Neovascular Age-Related Macular Degeneration. *N. Engl. J. Med.* **2006**, 1432–1444.
11. Rosenfeld, P. J.; Brown, D. M.; Heier, J. S.; Boyer, D. S.; Kaiser, P. K.; Chung, C. Y.; Kim, R. Y. Ranibizumab for Neovascular Age-Related Macular Degeneration. *N. Engl. J. Med.* **2006**, 1419–1431.
12. Bhisitkul, R. 7 Year Update on the Anchor/Marina Ranibizumab Cohort: The Seven Up Study. *2011 UCSF Ophthalmology Update (Dec. 2−3, 2011)*, San Francisco, CA, 2011.
13. Jackson, T. L.; Kirkpatrick, L. Cost Comparison of Ranibizumab and Bevacizumab. *BMJ* **2011**, d5058.
14. Singh, S. R.; Grossniklaus, H. E.; Kang, S. J.; Edelhauser, H. F.; Ambati, B. K.; Kompella, U. B. Intravenous Transferrin, Rgd Peptide and Dual-Targeted Nanoparticles Enhance Anti-Vegf Intraceptor Gene Delivery to Laser-Induced Cnv. *Gene Ther.* **2009**, 645–659.
15. Jani, P. D.; Singh, N.; Jenkins, C.; Raghava, S.; Mo, Y.; Amin, S.; Kompella, U. B.; Ambati, B. K. Nanoparticles Sustain Expression of Flt Intraceptors in the Cornea and Inhibit Injury-Induced Corneal Angiogenesis. *Invest. Ophthalmol. Visual Sci.* **2007**, 2030–2036.
16. Hsieh, W. J.; Liang, C. J.; Chieh, J. J.; Wang, S. H.; Lai, I. R.; Chen, J. H.; Chang, F. H.; Tseng, W. K.; Yang, S. Y.; Wu, C. C.; *et al.* In Vivo Tumor Targeting and Imaging with Anti-Vascular Endothelial Growth Factor Antibody-Conjugated Dextran-Coated Iron Oxide Nanoparticles. *Int. J. Nanomed.* **2012**, 2833–2842.
17. Singh, N.; Amin, S.; Richter, E.; Rashid, S.; Scoglietti, V.; Jani, P. D.; Wang, J.; Kaur, R.; Ambati, J.; Dong, Z.; *et al.* Flt-1 Intraceptors Inhibit Hypoxia-Induced Vegf Expression in Vitro and Corneal Neovascularization in Vivo. *Invest. Ophthalmol. Visual Sci.* **2005**, 1647–1652.
18. Halbert, C. L.; Miller, A. D.; McNamara, S.; Emerson, J.; Gibson, R. L.; Ramsey, B.; Aitken, M. L. Prevalence of Neutralizing Antibodies against Adeno-Associated Virus (Aav) Types 2, 5, and 6 in Cystic Fibrosis and Normal Populations: Implications for Gene Therapy Using Aav Vectors. *Hum. Gene Ther.* **2006**, 440–447.

19. Thomas, C. E.; Ehrhardt, A.; Kay, M. A. Progress and Problems with the Use of Viral Vectors for Gene Therapy. *Nat. Rev. Genet.* **2003**, 346–358.
20. Tweden, K. S.; Harasaki, H.; Jones, M.; Blevitt, J. M.; Craig, W. S.; Pierschbacher, M.; Helmus, M. N. Accelerated Healing of Cardiovascular Textiles Promoted by an Rgd Peptide. *J. Heart Valve Dis.* **1995**, S90–97.
21. Zahn, G.; Vossmeyer, D.; Stragies, R.; Wills, M.; Wong, C. G.; Loffler, K. U.; Adamis, A. P.; Knolle, J. Preclinical Evaluation of the Novel Small-Molecule Integrin Alpha5beta1 Inhibitor Jsm6427 in Monkey and Rabbit Models of Choroidal Neovascularization. *Arch. Ophthalmol.* **2009**, 1329–1335.
22. Santos, S. C.; Dias, S. Internal and External Autocrine Vegf/Kdr Loops Regulate Survival of Subsets of Acute Leukemia through Distinct Signaling Pathways. *Blood* **2004**, 3883–3889.
23. Nomura, M.; Yamagishi, S.; Harada, S.; Hayashi, Y.; Yamashima, T.; Yamashita, J.; Yamamoto, H. Possible Participation of Autocrine and Paracrine Vascular Endothelial Growth Factors in Hypoxia-Induced Proliferation of Endothelial Cells and Pericytes. *J. Biol. Chem.* **1995**, 28316–28324.
24. Rosenfeld, P. J.; Shapiro, H.; Tuomi, L.; Webster, M.; Elledge, J.; Blodi, B. Characteristics of Patients Losing Vision after 2 Years of Monthly Dosing in the Phase Iii Ranibizumab Clinical Trials. *Ophthalmology* **2011**, 523–530.
25. Gailit, J.; Clarke, C.; Newman, D.; Tonnesen, M. G.; Mosesson, M. W.; Clark, R. A. Human Fibroblasts Bind Directly to Fibrinogen at Rgd Sites through Integrin Alpha(V)Beta3. *Exp. Cell Res.* **1997**, 118–126.
26. Kotoh, K.; Nakamuta, M.; Kohjima, M.; Fukushima, M.; Morizono, S.; Kobayashi, N.; Enjoji, M.; Nawata, H. Arg-Gly-Asp (Rgd) Peptide Ameliorates Carbon Tetrachloride-Induced Liver Fibrosis *Via* Inhibition of Collagen Production and Acceleration of Collagenase Activity. *Int. J. Mol. Med.* **2004**, 1049–1053.
27. Qazi, Y.; Stagg, B.; Singh, N.; Singh, S.; Zhang, X.; Luo, L.; Simonis, J.; Kompella, U. B.; Ambati, B. K. Nanoparticle-Mediated Delivery of Shrna.Vegf-a Plasmids Regresses Corneal Neovascularization. *Invest. Ophthalmol. Visual Sci.* **2012**, 2837–2844.
28. Amrite, A. C.; Kompella, U. B. Size-Dependent Disposition of Nanoparticles and Microparticles Following Subconjunctival Administration. *J. Pharm. Pharmacol.* **2005**, 1555–1563.
29. Martin, D. F.; Maguire, M. G.; Fine, S. L.; Ying, G. S.; Jaffe, G. J.; Grunwald, J. E.; Toth, C.; Redford, M.; Ferris, F. L., 3rd Ranibizumab and Bevacizumab for Treatment of Neovascular Age-Related Macular Degeneration: Two-Year Results. *Ophthalmology* **2012**, 1388–1398.
30. Lou, L.; Uehara, H.; Zhang, X.; Olsen, T.; Das, S. K.; Holt, D.; Simonis, J. M.; Jackman, K.; Archer, B.; Sing, N.; *et al.* Photoreceptor Avascular Privilege is Shielded by Soluble VEGF Receptor-1. *eLife*, **2013**, in press.
31. Vasir, J. K.; Labhasetwar, V. Quantification of the Force of Nanoparticle-Cell Membrane Interactions and Its Influence on Intracellular Trafficking of Nanoparticles. *Biomaterials* **2008**, 4244–4252.
32. Wang, L. S.; Chen, Y. W.; Li, D. G.; Lu, H. M. Arg-Gly-Asp-Mannose-6-Phosphate Inhibits Activation and Proliferation of Hepatic Stellate Cells in Vitro. *World J. Gastroenterol.* **2006**, 1303–1307.
33. Xu, X. D.; Liang, L.; Chen, C. S.; Lu, B.; Wang, N. L.; Jiang, F. G.; Zhang, X. Z.; Zhuo, R. X. Peptide Hydrogel as an Intraocular Drug Delivery System for Inhibition of Postoperative Scarring Formation. *ACS Appl. Mater. Interfaces* **2010**, 2663–2671.
34. Amrite, A. C.; Edelhauser, H. F.; Singh, S. R.; Kompella, U. B. Effect of Circulation on the Disposition and Ocular Tissue Distribution of 20 Nm Nanoparticles after Periocular Administration. *Mol. Vision* **2008**, 150–160.
35. Singh, N.; Jani, P. D.; Suthar, T.; Amin, S.; Ambati, B. K. Flt-1 Intraceptor Induces the Unfolded Protein Response, Apoptotic Factors, and Regression of Murine Injury-Induced Corneal Neovascularization. *Invest. Ophthalmol. Visual Sci.* **2006**, 4787–4793.
36. Ahlers, C.; Golbaz, I.; Stock, G.; Fous, A.; Kolar, S.; Pruente, C.; Schmidt-Erfurth, U. Time Course of Morphologic Effects on Different Retinal Compartments after Ranibizumab Therapy in Age-Related Macular Degeneration. *Ophthalmology* **2008**, e39–46.
37. Bellerive, C.; Cinq-Mars, B.; Lalonde, G.; Malenfant, M.; Tourville, E.; Tardif, Y.; Giasson, M.; Hebert, M. Bevacizumab and Ranibizumab for Neovascular Age-Related Macular Degeneration: A Treatment Approach Based on Individual Patient Needs. *Can. J. Ophthalmol.* **2012**, 165–169.
38. Marneros, A. G.; Fan, J.; Yokoyama, Y.; Gerber, H. P.; Ferrara, N.; Crouch, R. K.; Olsen, B. R. Vascular Endothelial Growth Factor Expression in the Retinal Pigment Epithelium Is Essential for Choriocapillaris Development and Visual Function. *Am. J. Pathol.* **2005**, 1451–1459.
39. Kurihara, T.; Westenskow, P. D.; Bravo, S.; Aguilar, E.; Friedlander, M. Targeted Deletion of Vegfa in Adult Mice Induces Vision Loss. *J. Clin. Invest.* **2012**, 4213–4217.
40. Murakami, Y.; Ikeda, Y.; Yonemitsu, Y.; Miyazaki, M.; Inoue, M.; Hasegawa, M.; Sueishi, K.; Ishibashi, T. Inhibition of Choroidal Neovascularization *Via* Brief Subretinal Exposure to a Newly Developed Lentiviral Vector Pseudotyped with Sendai Viral Envelope Proteins. *Hum. Gene Ther.* **2010**, 199–209.
41. Nishijima, K.; Ng, Y. S.; Zhong, L.; Bradley, J.; Schubert, W.; Jo, N.; Akita, J.; Samuelsson, S. J.; Robinson, G. S.; Adamis, A. P.; *et al.* Vascular Endothelial Growth Factor-a Is a Survival Factor for Retinal Neurons and a Critical Neuroprotectant During the Adaptive Response to Ischemic Injury. *Am. J. Pathol.* **2007**, 53–67.
42. Quaggin, S. E. Turning a Blind Eye to Anti-Vegf Toxicities. *J. Clin. Invest.* **2012**, 3849–3851.
43. Saint-Geniez, M.; Maharaj, A. S.; Walshe, T. E.; Tucker, B. A.; Sekiyama, E.; Kurihara, T.; Darland, D. C.; Young, M. J.; D'Amore, P. A. Endogenous Vegf Is Required for Visual Function: Evidence for a Survival Role on Muller Cells and Photoreceptors. *PLoS One* **2008**, e3554.
44. Takeda, A.; Baffi, J. Z.; Kleinman, M. E.; Cho, W. G.; Nozaki, M.; Yamada, K.; Kaneko, H.; Albuquerque, R. J.; Dridi, S.; Saito, K.; *et al.* Ccr3 Is a Target for Age-Related Macular Degeneration Diagnosis and Therapy. *Nature* **2009**, 225–230.
45. Goody, R. J.; Hu, W.; Shafiee, A.; Struharik, M.; Bartels, S.; Lopez, F. J.; Lawrence, M. S. Optimization of Laser-Induced Choroidal Neovascularization in African Green Monkeys. *Exp. Eye Res.* **2011**, 464–472.
46. Redfern, W. S.; Storey, S.; Tse, K.; Hussain, Q.; Maung, K. P.; Valentin, J. P.; Ahmed, G.; Bigley, A.; Heathcote, D.; McKay, J. S. Evaluation of a Convenient Method of Assessing Rodent Visual Function in Safety Pharmacology Studies: Effects of Sodium Iodate on Visual Acuity and Retinal Morphology in Albino and Pigmented Rats and Mice. *J. Pharmacol. Toxicol. Methods* **2011**, 102–114.
47. Cho, Y. K.; Uehara, H.; Young, J. R.; Tyagi, P.; Kompella, U. B.; Zhang, X.; Luo, L.; Singh, N.; Archer, B.; Ambati, B. K. Flt23k Nanoparticles Offer Additive Benefit in Graft Survival and Anti-Angiogenic Effects When Combined with Triamcinolone. *Invest. Ophthalmol. Visual Sci.* **2012**, *53*, 2328–2336.
48. Furino, C.; Ferrara, A.; Cardascia, N.; Besozzi, G.; Alessio, G.; Sborgia, L.; Boscia, F. Combined Cataract Extraction and Intravitreal Bevacizumab in Eyes with Choroidal Neovascularization Resulting from Age-Related Macular Degeneration. *J. Cataract Refract. Surg.* **2009**, 1518–1522.
49. Ruggeri, M.; Tsechpenakis, G.; Jiao, S.; Jockovich, M. E.; Cebulla, C.; Hernandez, E.; Murray, T. G.; Puliafito, C. A. Retinal Tumor Imaging and Volume Quantification in Mouse Model Using Spectral-Domain Optical Coherence Tomography. *Opt. Express* **2009**, 4074–4083.
50. Schmucker, C.; Schaeffel, F. A Paraxial Schematic Eye Model for the Growing C57bl/6 Mouse. *Vision Res.* **2004**, 1857–1867.